The Astrophysical Journal, 767:146 (14pp), 2013 April 20 doi:10.1088/0004-637X/767/2/146
© 2013. The American Astronomical Society. All rights reserved. Printed in the U.S.A.

THE COSMOGRID SIMULATION: STATISTICAL PROPERTIES OF SMALL DARK MATTER HALOS

Tomoaki Ishiyama[1], Steven Rieder[2,3], Junichiro Makino[4,5], Simon Portegies Zwart[2], Derek Groen[6], Keigo Nitadori[5], Cees de Laat[3], Stephen McMillan[7], Kei Hiraki[8], and Stefan Harfst[9]
[1] Center for Computational Science, University of Tsukuba, 1-1-1, Tennodai, Tsukuba, Ibaraki 305-8577, Japan; ishiyama@ccs.tsukuba.ac.jp
[2] Sterrewacht Leiden, Leiden University, P.O. Box 9513, 2300-RA Leiden, The Netherlands
[3] Section System and Network Engineering, University of Amsterdam, Amsterdam, The Netherlands
[4] Graduate School of Science and Engineering, Tokyo Institute of Technology, Japan
[5] RIKEN Advanced Institute for Computational Science, Japan
[6] Centre for Computational Science, Department of Chemistry, University College London, 20 Gordon Street, London, WC1H 0AJ, UK
[7] Department of Physics, Drexel University, Philadelphia, PA 19104, USA
[8] Department of Creative Informatics, Graduate School of Information Science and Technology, the University of Tokyo, Japan
[9] Center for Astronomy and Astrophysics, Technical University Berlin, Hardenbergstr. 36, D-10623 Berlin, Germany
Received 2011 January 10; accepted 2013 March 5; published 2013 April 5

ABSTRACT

We present the results of the "Cosmogrid" cosmological *N*-body simulation suites based on the concordance LCDM model. The Cosmogrid simulation was performed in a 30 Mpc box with 2048^3 particles. The mass of each particle is $1.28 \times 10^5\ M_\odot$, which is sufficient to resolve ultra-faint dwarfs. We found that the halo mass function shows good agreement with the Sheth & Tormen fitting function down to $\sim 10^7\ M_\odot$. We have analyzed the spherically averaged density profiles of the three most massive halos which are of galaxy group size and contain at least 170 million particles. The slopes of these density profiles become shallower than -1 at the innermost radius. We also find a clear correlation of halo concentration with mass. The mass dependence of the concentration parameter cannot be expressed by a single power law, however a simple model based on the Press–Schechter theory proposed by Navarro et al. gives reasonable agreement with this dependence. The spin parameter does not show a correlation with the halo mass. The probability distribution functions for both concentration and spin are well fitted by the log-normal distribution for halos with the masses larger than $\sim 10^8\ M_\odot$. The subhalo abundance depends on the halo mass. Galaxy-sized halos have 50% more subhalos than $\sim 10^{11}\ M_\odot$ halos have.

Key words: cosmology: theory – dark matter – galaxies: dwarf – methods: numerical

Online-only material: color figures

1. INTRODUCTION

According to the present standard LCDM model, the universe is thought to be composed primarily of cold dark matter (CDM) and dark energy (White & Rees 1978; Peacock 1999). Structure formation of the universe proceeds hierarchically in this model. Smaller-scale structures collapse first, and then merge into larger-scale structures.

There is serious discrepancy between the distribution of subhalos in galaxy-sized halos obtained by numerical simulations and the observed number of dwarf galaxies in the Local Group (Klypin et al. 1999; Moore et al. 1999a). This "missing dwarf problem" is still considered to be one of the most serious problems in the CDM paradigm (e.g., Kroupa et al. 2010). In order to understand the origin of this discrepancy, it is necessary to perform high-resolution cosmological *N*-body simulations and obtain unbiased samples of galaxy-sized halos with resolution high enough to obtain reliable statistics of subhalos since the subhalo abundance shows large halo-to-halo variations (Ishiyama et al. 2009b).

Cosmological *N*-body simulations have been widely used to study the nonlinear structure formation of the universe and have been an important tool for a better understanding of our universe. In order to study the spatial correlation of galaxies, the first cosmological *N*-body simulations were performed in the 1970s using approximately 1000 particles (e.g., Miyoshi & Kihara 1975; Fall 1978; Aarseth et al. 1979; Efstathiou 1979). Since then, the development of better simulation algorithms and improvements in the performance of computers allow us to use much larger numbers of particles and have drastically increased the resolution of cosmological simulations.

Today, it is not uncommon that the number of particles exceeds 10^9 in high-resolution simulations. In these works, the size of the simulation volumes is typically $[O(\mathrm{Gpc})]^3$ and populations of galaxy clusters, gravitational lensing, and the baryon acoustic oscillation are studied (e.g., Evrard et al. 2002; Wambsganss et al. 2004; Teyssier et al. 2009; Kim et al. 2009; Crocce et al. 2010). The simulation results are also used to construct mock halo catalogs for next generation large volume surveys. Others use simulations of $[O(100\,\mathrm{Mpc})]^3$ volumes to study the internal properties of galaxy-sized dark matter halos, their formation, evolution, and statistical properties (e.g., Springel et al. 2005; Klypin et al. 2011; White et al. 2010).

Using the results of high-resolution simulations of small-scale structures, we can study the fine structures of galactic halos, the distribution of subhalos, their structures, and their dependence on the nature of dark matter. This information has a strong impact on the indirect search for dark matter since gamma-ray flux by self-annihilation is proportional to local density if we consider neutralino as the candidate of dark matter. Thus, we can restrict the nature of dark matter using the results of high-resolution simulations of small-scale structures and indirect searches of dark matter. In addition, galaxies are considered to form in dark matter halos with a mass larger than a critical value (Strigari et al. 2008; Li et al. 2009; Macciò et al. 2009; Okamoto & Frenk 2009). The structure of smallest halos which can host galaxies is important for the understanding of the galaxy formation processes.

The simulation of smaller-scale structures of dark matter halos is not a trivial task since a very wide dynamic range of space, mass, and time must be covered. In particular, the number of time steps of such simulations is significantly larger than that of larger-scale simulations since the dynamical timescale is proportional to $1.0/\sqrt{G\bar{\rho}}$, where $\bar{\rho}$ is the local density. Structures of smaller scales form earlier, and thus have higher densities, therefore, simulations of smaller scales are computationally more expensive.

Recently, simulations with galactic halos of very high resolution have been performed (Diemand et al. 2008; Springel et al. 2008; Stadel et al. 2009). These works used the re-simulation method, where one selects one or a few halos at $z = 0$ from a simulation which covers a large volume (typically a cube of size O(100 Mpc)) with a relatively low resolution. The corresponding regions of these halos are then identified in the initial particle distribution, and the particles in these regions are replaced by a larger number of smaller particles. After this is done, the entire volume is simulated to $z = 0$ again.

With this re-simulation method, we can resolve the structures of selected halos with extremely high resolution (Diemand et al. 2008; Springel et al. 2008; Stadel et al. 2009). However, this method cannot be used for the study of halo-to-halo variations. Different halos are born in different environments and grow differently. The difference in the environment and growth history must be the cause of halo-to-halo variations. Therefore, in order to study variations, we need a bias-free set of a large number of halos. Clearly one cannot obtain a large number of halos with the re-simulation method in practical time.

In principle, one can improve the statistics by increasing the number of halos selected for re-simulations. In order to avoid the selection bias, we need to apply random, bias-free selection, and the most reliable bias-free selection is to select all halos, in other words, to simulate the entire simulation box with uniformly high-mass resolution. Ishiyama et al. (2009b) performed the first bias-free high-resolution simulation of small-scale structures. They analyzed the statistics of the subhalo abundance using the complete set of halos in the simulation box. The number of particles was 1600^3 in a 46.5 Mpc cubic box and the mass of a particle was $10^6\,M_\odot$. The subhalo abundance showed large halo-to-halo variations (see also Ishiyama et al. 2008; Boylan-Kolchin et al. 2010). The concentration parameter and the radius at the moment of the maximum expansion showed a fairly tight correlation with the subhalo abundance. Halos formed earlier have a smaller number of subhalos at present. This correlation suggests that the difference in the formation history is the origin of the variation of the subhalo abundance (see also Gao et al. 2004; van den Bosch et al. 2005; Zentner et al. 2005).

The Millennium-II simulation (Boylan-Kolchin et al. 2009) used a 137 Mpc cubic box and the particle mass of $\sim 9.45 \times 10^6\,M_\odot$. Its result is suitable for the analysis of the statistics of galaxy-sized dark matter halos, because the number of halos is larger than that of Ishiyama et al. (2009b). However, due to the lack of the mass resolution, it cannot be used to study the statistics of dwarf-galaxy-sized halos and the statistics of subhalos with size larger than faint dwarf galaxies.

In this paper, we describe the first result of our Cosmogrid simulation. We simulated the evolution of halos in a 30 Mpc cubic box using 2048^3 particles. The mass of one particle is $1.28 \times 10^5\,M_\odot$. The resolution reaches down to ultra-faint dwarf-galaxy-sized halos ($\sim 10^7\,M_\odot$) and is more than eight times better than that of our previous simulation (Ishiyama et al. 2009b). We focus on the halo mass function with the mass down to $10^7\,M_\odot$, the structures of most massive halos, and statistics of the internal properties of dwarf-galaxy-sized halos. We describe our initial conditions and numerical settings in Section 2, and results in Section 3. We discuss and summarize our results in Section 4.

Table 1
Run Parameters

Name	N	L (Mpc)	ε (pc)	m ($M_\odot$)
CG2048	2048^3	30.0	175	1.28×10^5
CG1024	1024^3	30.0	350	1.03×10^6
CG512	512^3	30.0	700	8.21×10^6
IFM2009 (Ishiyama et al. 2009b)	1600^3	46.5	700	1.00×10^6

Note. Here, N, L, ε, and m are the total number of particles, the box length, the softening length, and the mass resolution.

2. INITIAL CONDITIONS AND NUMERICAL METHOD

The cosmological parameters adopted are based on the concordance LCDM cosmological model ($\Omega_0 = 0.3$, $\lambda_0 = 0.7$, $h = 0.7$, $\sigma_8 = 0.8$, $n = 1.0$). These values are the same as those used in our previous simulation (Ishiyama et al. 2009b). We used a periodic cube of the comoving size of 30 Mpc. The number of particles for the largest run is 2048^3 which corresponds to a mass resolution of $1.28 \times 10^5\,M_\odot$. To generate the initial particle distributions, we used the MPGRAFIC package (Prunet et al. 2008), which is a parallelized variation of the GRAFIC package (Bertschinger 2001). The initial red was 65.

In order to investigate the effect of the mass and spatial resolution, we performed two simulations with lower resolution. We generated the initial conditions for these low-resolution runs (CG1024 and CG512) by replacing 8 or 64 particles in the high-resolution initial condition (CG2048) with a single particle 8 or 64 times more massive. We did not use any smoothing filter for density and velocity spaces. The massive particles were picked up at regular intervals before performing the Zel'dovich approximation. This procedure introduces some aliasing noise in the high frequency limit of CG1024 and CG512 runs. The corresponding halo contains less than a few hundred particles. However, here we use CG1024 and CG512 runs for only convergence studies, and analyze halos with more than $\sim$1000 particles. Thus, the effect of the aliasing noise should be negligible. In Table 1, we summarize parameters used in our simulations.

We used a leapfrog integrator with shared and adaptive time steps. The step size was determined as $\min(2.0\sqrt{\varepsilon/|\boldsymbol{a}_i|}, 2.0\varepsilon/|\boldsymbol{v}_i|)$ (minimum of these two values for all particles). All particles have the same timesteps. The gravitational plummer softening length ε was 175 pc at $z = 0$. The softening was constant in comoving coordinates from $z = 65$ (initial condition) to $z = 10$. From $z = 10$ to $z = 0$, it was constant in physical coordinates. This procedure is similar to that used in Kawai et al. (2004).

For the largest simulation, we used four supercomputers. Three of them are Cray XT4 machines at the Center for Computational Astrophysics of National Astronomical Observatory of Japan, the Edinburgh Parallel Computing Center in Edinburgh (United Kingdom) and IT Center for Science in Espoo (Finland). The fourth machine is an IBM pSeries 575 at SARA in Amsterdam (the Netherlands). Part of the calculation was done in a "grid" computing environment, in which we used

Table 2
Global Parameters of Three Most Massive Group Sized Halos at $z = 0$

Name	Run	M ($10^{13}\ M_\odot$)	N	$R_{\rm vir}$ (kpc)	$R_{\rm vmax}$ (kpc)	$V_{\rm max}$ (km s^{-1})
GP1	CG2048	5.24	408499843	969	200	596
	CG1024	5.19	50632942	966	186	589
	CG512	5.22	6361253	968	184	596
GP2	CG2048	3.58	279382586	854	305	476
	CG1024	3.57	34836692	853	279	472
	CG512	3.57	4347651	852	294	475
GP3	CG2048	2.25	175752770	731	178	434
	CG1024	2.26	22072073	732	187	431
	CG512	2.25	2746874	731	192	434

Notes. Here, M, N, $R_{\rm vir}$, $R_{\rm vmax}$, and $V_{\rm max}$ are the mass, the number of particles, the virial radius in which the spherical overdensity is 101 times the critical value, the radius where the rotation velocity is maximum, and the maximum rotation velocity, respectively.

more than one machine simultaneously for one run (Portegies Zwart et al. 2010).

For the time integration we used the GreeM code (Ishiyama et al. 2009a) for single supercomputer runs and the SUSHI code (Groen et al. 2011) for multi-supercomputer runs. The GreeM code is a massively parallel TreePM code based on the parallel TreePM code of Yoshikawa & Fukushige (2005) for large cosmological N-body simulations. The long range forces are calculated by the Particle-Mesh (PM) method (Hockney & Eastwood 1981), and the short range forces are calculated by the Barnes–Hut–Tree method (Barnes & Hut 1986). Yoshikawa & Fukushige (2005) used a 1-D slab decomposition, but in GreeM we use a 3-D multi-section decomposition (Makino 2004) to improve its scalability. In addition, the decomposition is based on CPU time measurement, so that near ideal load balance is archived. The SUSHI code is an extension of the GreeM code which can run concurrently on multiple supercomputers. It uses the MPWide communication library (Groen et al. 2010) to facilitate message passing between distributed supercomputers. We used 512^3 PM grid points for PM calculations, the opening angle for the tree method was 0.3 from initial to $z = 10$, and 0.5 from $z = 10$ to $z = 0$.

The calculation time was ∼180 s per step with 1024 cpu cores for the largest run on the Cray XT4 in Japan and ∼140 s per step with 2048 cpu cores on the IBM pSeries 575 in the Netherlands. We spent about 3.5 million CPU hours to perform all the 60,283 steps in our simulation.

We used the spherical overdensity method (Lacey & Cole 1994) to identify halos and calculated the halo virial radius $R_{\rm vir}$. The virial radius of a halo is defined as the radius in which the spherical overdensity is $\Delta(z)$ times the critical value. The overdensity $\Delta(z)$ is given by the analytic formula (Bryan & Norman 1998),

$$\Delta(z) = (18\pi^2 + 82x - 39x^2)/\Omega(z), \quad (1)$$

where $x \equiv \Omega(z) - 1$. The mass of a halo is defined as interior mass within the virial radius.

The mass of the most massive halo is $5.24 \times 10^{13}\ M_\odot$. It contains 4.08×10^8 particles. Via Lactea I, II (Diemand et al. 2007, 2008), and Aquarius simulations (Springel et al. 2008) used $\sim 10^8$, $\sim 5 \times 10^8$, and $\sim 10^9$ particles for the largest halo. Table 2 shows the properties of the three most massive halos in our simulation.

The subhalo finder is the same as that described in Ishiyama et al. (2009b). Our method is based on the idea of finding all local potential minima. Initially, all particles are candidates for the centers of halos. We then search for the particle with the smallest (most negative) potential and regard it as the center of a halo. We then exclude $n_{\rm min}$ neighbor particles of this particle from the list of remaining particles, and search the particle with the smallest potential from the list. At this time, we again search $n_{\rm min}$ neighbor particles from the list of originally selected particles, and if the potential of one neighbor is smaller, we do not add this particle to the list of halos. However, we remove $n_{\rm min}$ neighbors no matter whether the particle is added to the list or not. We repeat this procedure until there is no remaining particle. We set $n_{\rm min}$ so that $n_{\rm min} \times m = 1.0 \times 10^7\ M_\odot$, where m is the mass of each particle.

Figure 1 shows the snapshots at $z = 0$. In Figure 2, we also present the time evolution of the whole box and that of the most massive halo. The three most massive halos in simulations with three different resolutions are shown in Figure 3. The positions of subhalos agree very well in three simulations. Of course, there are some discrepancies near the centers of halos. In particular, whereas there is only one core in the center of the second massive halo (GP2) of CG2048, there are two cores in GP2 of CG1024 and CG512.

The reason of this difference is that the formation history of this halo is rather violent. It experienced many mergers near $z = 0$ in the center of the halo and is far from the relaxed state. The difference of the accuracy of integration changed the timescale of the mergers of the halos with three different resolutions. At $z = 0$, the halo GP2 has just completed the merger in the CG2048 run, whereas the same merger event is still on-going in CG1024 and CG512 runs. If we consider the spherically averaged density profile of the halo, the difference becomes important (see Section 3.2).

3. RESULTS

3.1. Mass Function

Press & Schechter (1974) established a recipe to derive the number of dark matter halos based on the hierarchical clustering model. Since then, a number of analytic formulae for the mass function have been proposed. Many of them are designed to give a good agreement with results of high-resolution N-body simulations (e.g., Sheth & Tormen 1999; Jenkins et al. 2001; Reed et al. 2003; Yahagi et al. 2004; Warren et al. 2006; Tinker et al. 2008, and references therein).

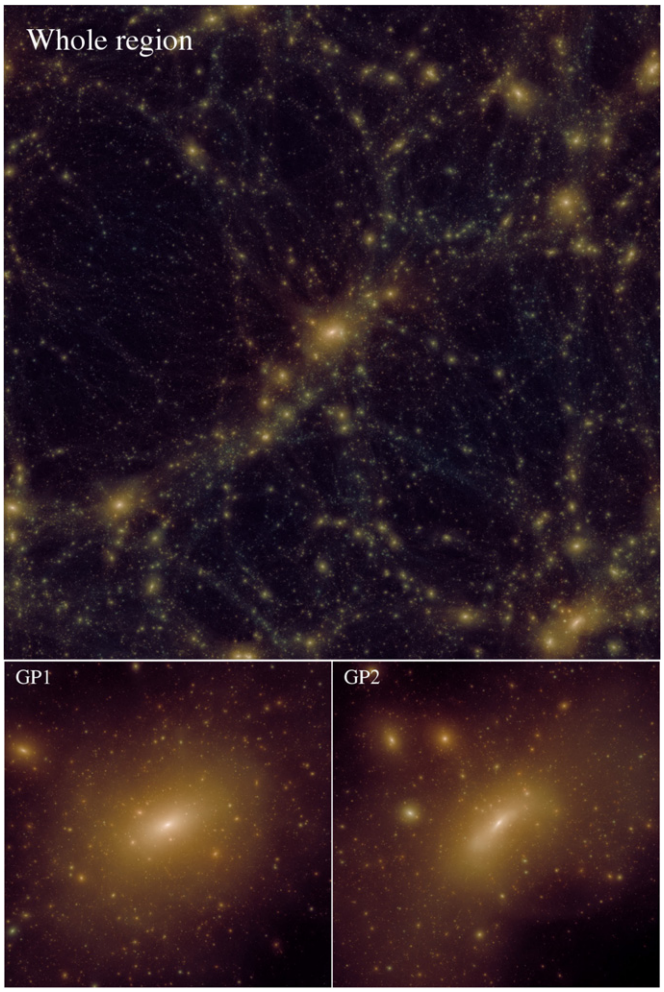

Figure 1. Projected density of dark matter at $z = 0$ in our largest simulation (2048^3 particles). Top panel shows the whole region with the volume of $(30\,\mathrm{Mpc})^3$. Bottom panels show the projected density of the two most massive group-sized halos. These volumes are $(2\,\mathrm{Mpc})^3$.

(A color version of this figure is available in the online journal.)

These formulae can reproduce the mass function between $10^{10}\,M_\odot$ and cluster scale very well. Here, we examine the mass function of mass below $10^{10}\,M_\odot$ down to $10^7\,M_\odot$. The mass function of this range has been studied only in high redshift (e.g., Reed et al. 2007; Lukić et al. 2007).

Figure 4 shows the halo mass functions at three different redshifts for the CG2048 run and the prediction of the Sheth & Tormen formula (ST, Sheth & Tormen 1999). The agreement is very good for the mass from $\sim 10^7\,M_\odot$ to $M = 1.0 \times 10^{13}\,M_\odot$ at $z = 0$. The difference is less than 10% for $M = 5.0 \times 10^7\,M_\odot$ to $M = 2.0 \times 10^{12}\,M_\odot$ at $z = 0$, $M = 5.0 \times 10^7\,M_\odot$ to $M = 5.0 \times 10^{10}\,M_\odot$ at $z = 3$, and $M = 8.0 \times 10^7\,M_\odot$ to $M = 4.0 \times 10^9\,M_\odot$ at $z = 5.4$.

Our results imply that the mass function is well represented by the ST function down to $10^7\,M_\odot$. However, our simulations have a slightly larger number of halos than the number predicted by the ST formula in particular at the high-mass end of the $z = 5.4$ mass function. Note that the finite volume of our simulation (the box length is 30 Mpc) might affect the mass function in some degrees. The absence of long-wavelength perturbations might increase the number of intermediate mass halos by about 10% (Bagla & Prasad 2006; Power & Knebe 2006). In order to test the effect of the box size, we performed additional simulations of 30, 45, and 60 Mpc boxes with 512^3 particles. The left panel of Figure 5 shows mass functions of these simulations at $z = 5.4$ relative to the ST formula. The difference becomes larger as the halo mass and the box size increase. The right panel of Figure 5 shows mass functions relative to the 30 Mpc simulation. We can see that the number of halos of the 30 Mpc box simulation is systematically larger than those of the 45 Mpc and 60 Mpc box simulations. The mass functions of the 45 Mpc and 60 Mpc box simulations are well converged for halos larger than $2.0 \times 10^{10}\,M_\odot$, which is the limit of resolution for the 60 Mpc box simulation. We can conclude that the larger number of halos seen in CG2048 at the high-mass end is caused by the absence of long-wavelength perturbations.

3.2. Density Structures of Most Massive Halos

Many groups have studied the density profile of dark matter halos using high-resolution cosmological *N*-body simulations (e.g., Navarro et al. 1997, 2004, 2010; Fukushige & Makino 1997, 2001, 2003; Moore et al. 1999b; Ghigna et al. 2000; Jing & Suto 2000, 2002; Jing 2000; Klypin et al. 2001; Taylor & Navarro 2001; Power et al. 2003; Fukushige et al. 2004; Diemand et al. 2004, 2005, 2008; Hayashi et al. 2004; Reed et al. 2005; Kazantzidis et al. 2006; Merritt et al. 2006; Gao et al. 2008; Stadel et al. 2009). In most of the recent works, the slopes of radial density profiles were around -1 in the inner region and around -3 in the outer region. The slope of density became shallower as the radius becomes smaller. Thus, the central slope is not described by any single power. Furthermore, the density profile was not universal. In other words, the slope showed a significant halo-to-halo scatter.

Recent studies (Stadel et al. 2009; Navarro et al. 2010) based on high-resolution simulations of galactic halos showed that the slopes of density became less than -1 at the radius 0.001 times the virial radius of the halo as predicted by early works (e.g., Graham et al. 2006). The Einasto profile showed better agreement than the Navarro–Frenk–White (NFW) profile (Navarro et al. 1997) which has been widely used for modeling dark matter halos because of its simplicity.

Almost all recent high-resolution simulations of single halos used galaxy-sized halos. Therefore, little is known if these findings can be applied to halos of different masses. Here, we present the density profiles of the three most massive halos in our simulation. These halos are galactic group-sized ones, with the mass of 5.24, 3.58, and $2.25 \times 10^{13}\,M_\odot$. They contain 408, 279, and 176 million particles.

The top panel of Figure 6 shows the spherically averaged density profiles of these halos at $z = 0$. We can see that the results of three simulations with different resolution are indistinguishable for radii larger than the reliability limits, except for the second massive halo. We calculated the reliability limits using criteria proposed by Fukushige & Makino (2001) and Power et al. (2003). We cannot ignore the effects of the local two-body relaxation for radii smaller than these limits. As can be seen in Figure 3, the slight difference of the merging epoch of the central cores caused this difference.

The slopes of density profiles become gradually shallower as the radius becomes smaller. The left panel of Figure 7 shows the slopes of density profiles of the most massive halo. As in the case of the density profile itself, the slopes also agree well with each other. The right panel of Figure 7 shows the slopes of the three most massive halos in the CG2048 run.

These profiles are significantly different from those of galactic halos in other recent high-resolution simulations, even if the

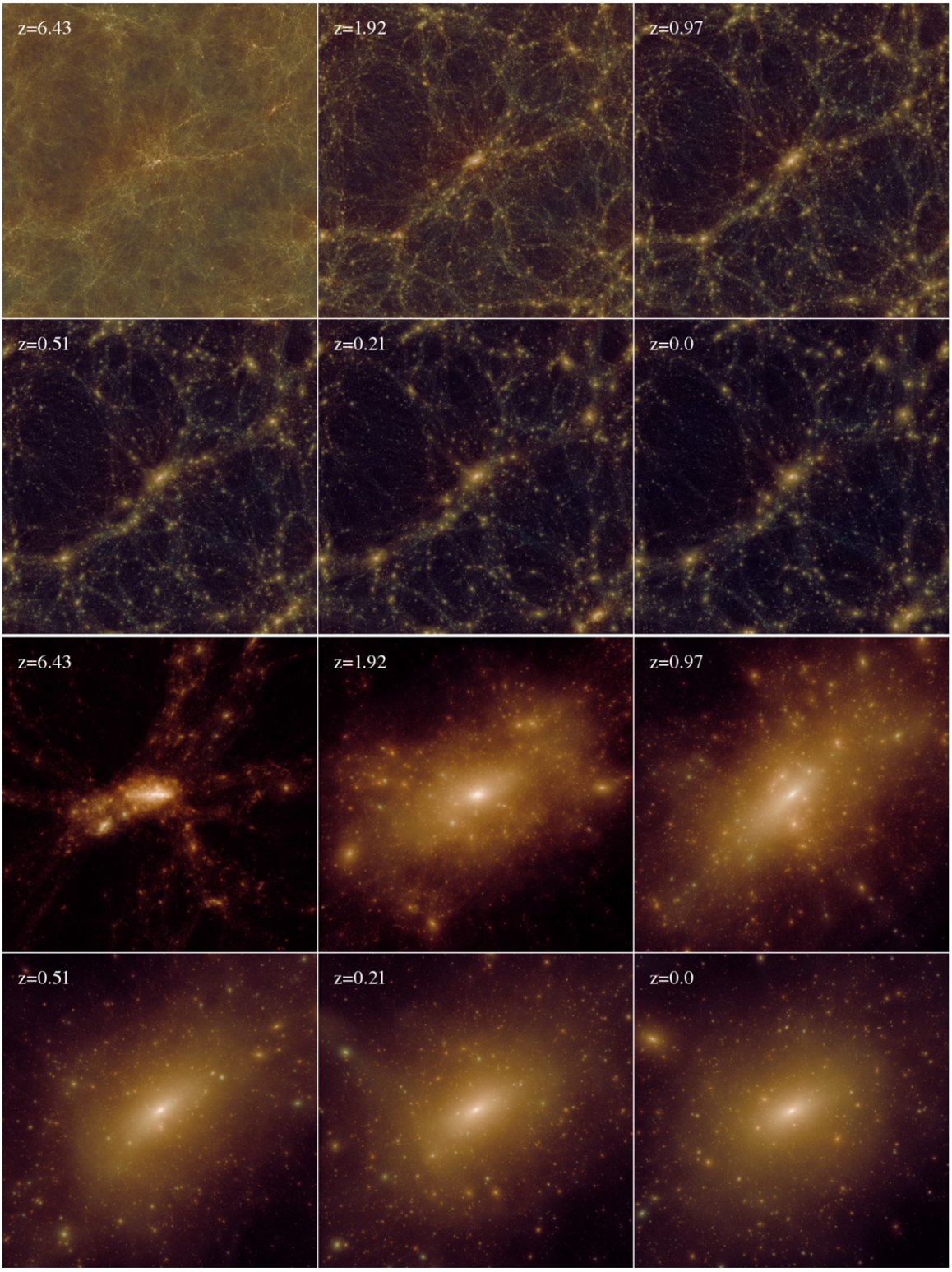

Figure 2. Evolution pictures of our largest simulation. Top six panels show the evolution of the whole region. Bottom six panels show the evolution of the most massive halo.

(A color version of this figure is available in the online journal.)

halo mass is scaled to be the same. The mass of the halos of the Aquarius simulation (Springel et al. 2008) or GHALO simulation (Stadel et al. 2009) is $\sim 10^{12}\ M_{\odot}$, which is an order of magnitude smaller than our three halos. The slope at $0.001\,R_{\rm vir}$ is -0.9 to -1.0 for our three halos. This value is in excellent agreement with the result of both simulations. Both of them gave the slope -1.0 for $r = 0.001 r_{200}$. This agreement does not mean the density profile obtained by these simulations and those by our simulation are identical. The concentration parameter, which we define here as $c_{\rm vmax} = R_{\rm vir}/R_{\rm vmax}$, is 4.8, where $R_{\rm vir}$ and $R_{\rm vmax}$ are the halo virial radius and the radius of the maximum rotational velocity. This value is significantly smaller

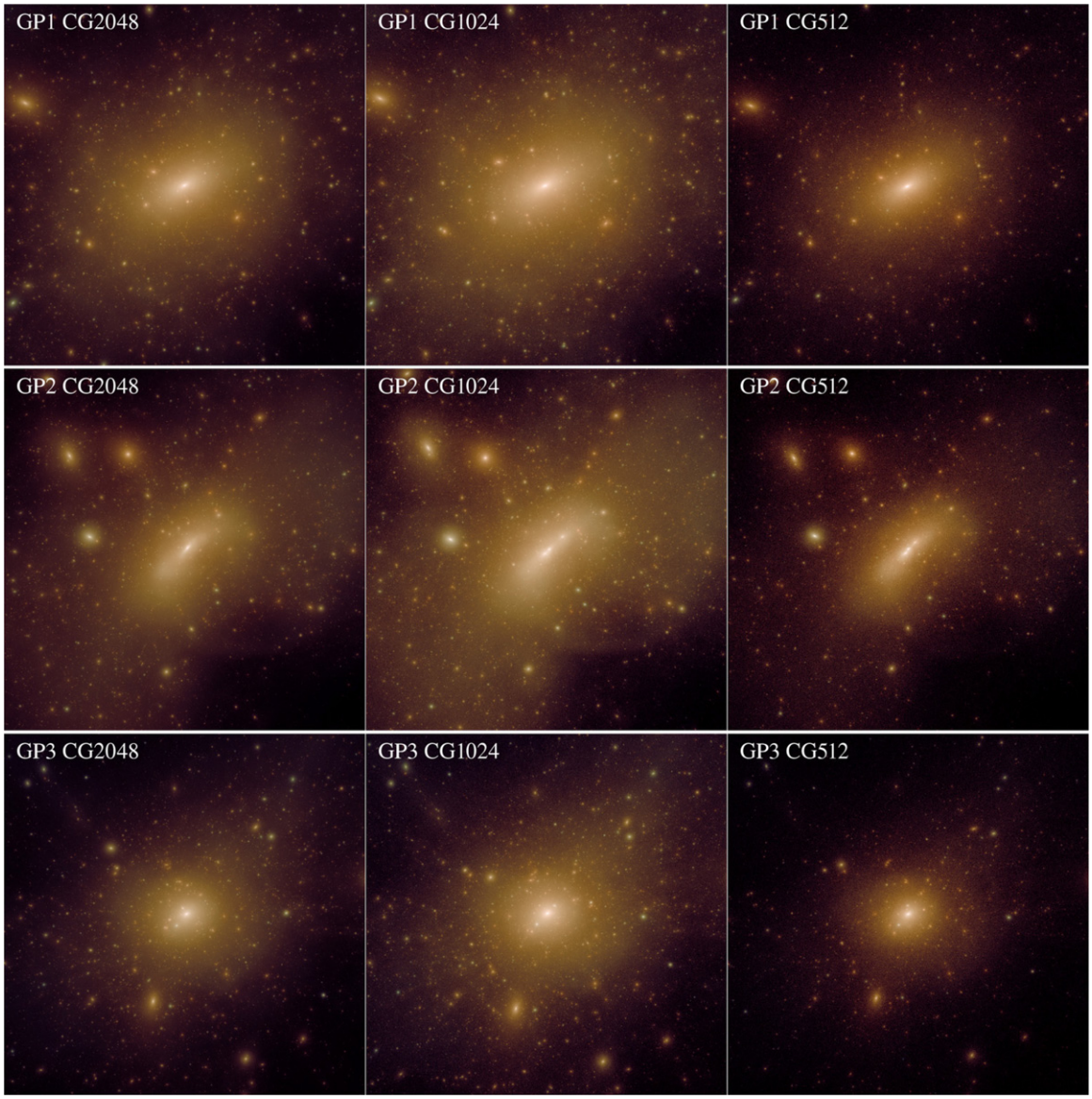

Figure 3. Projected density of dark matter at $z = 0$. Each row shows one of the three most massive halos with mass decreasing from top to bottom. Columns show different resolution from highest (left) to lowest (right).

(A color version of this figure is available in the online journal.)

than that of the Aquarius A-1 halo. Thus, the Aquarius halo is significantly more centrally concentrated, and yet the slope at $r = 0.001R_{\rm vir}$ is the same. Thus the rate of the shallowing of the slope is somewhat faster for the Aquarius halo than for our CG2048 halos. Most likely, this difference is due to the difference in the mass of the halo.

3.3. Concentration Distributions

The concentration parameter has been widely used to describe the internal structure of halos since it is tightly correlated with the formation epoch (Wechsler et al. 2002). Usually, the concentration is parameterized assuming that the density profiles of halos can be fitted by the NFW profile (Navarro et al. 1997),

$$\rho(r) = \frac{\rho_0}{(r/r_{\rm s})(1 + r/r_{\rm s})^2}, \qquad (2)$$

where ρ_0 is a characteristic density and r_s is a scale radius. The concentration $c_{\rm NFW} = R/r_s$ is widely used (e.g., Bullock et al. 2001b; Zhao et al. 2003, 2009; Macciò et al. 2007, 2008; Neto et al. 2007; Muñoz-Cuartas et al. 2011). It is known that $c_{\rm NFW}$ depends weakly on the halo mass. Halos with higher mass have smaller concentration, since the average density of a halo reflects the cosmic density at its formation time. The dependence is weaker for higher redshift (Zhao et al. 2003).

The concentration based on the NFW profile is affected by fitting ranges and resolution (Neto et al. 2007). Furthermore, recent high-resolution simulations showed that the density profile is significantly different from the NFW profile (Stadel et al. 2009; Navarro et al. 2010, also see Section 3.2). Thus, the use of $c_{\rm nfw}$ might cause some systematic bias (Gao et al. 2008; Reed et al. 2011).

We use the concentration $c_{\rm vmax}$ defined in Section 3.2, which is a simpler quantity to measure the concentration. Note that $R_{\rm vmax}$ can be easily determined directly from spherically averaged mass distribution without the need of any fitting formulae. If the density profile is represented by the NFW profile, either concentration can be converted to the other.

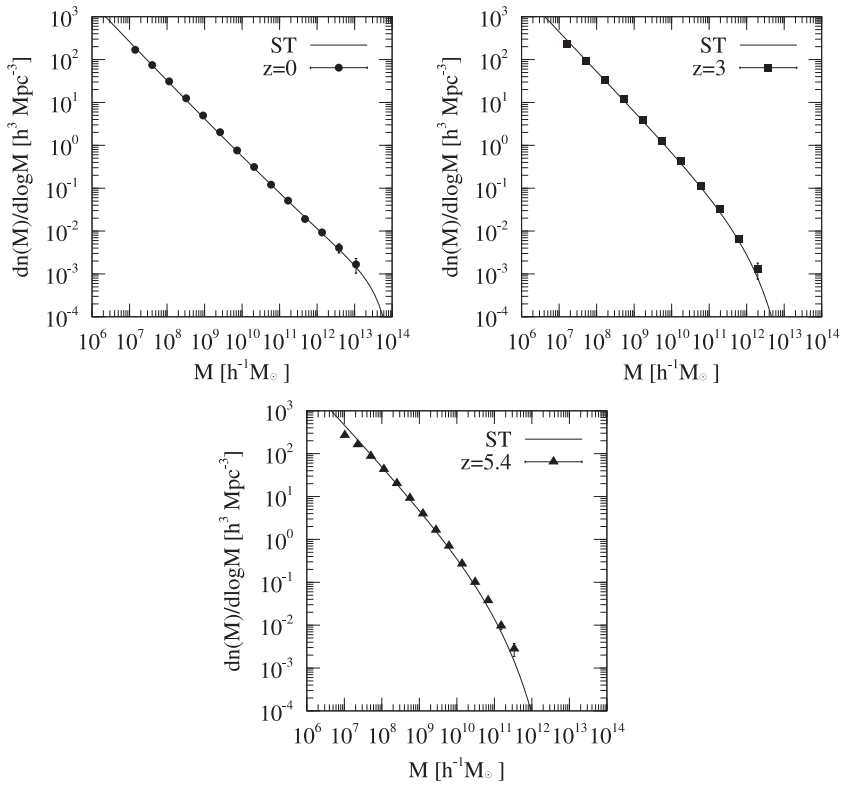

Figure 4. Mass function of our largest simulation (CG2048). The results of $z = 0.0$ (top-left), $z = 3.0$ (top-right), and $z = 5.4$ (bottom) are shown. Solid curves are the Sheth & Tormen (1999) function. Error bars are Poisson errors.

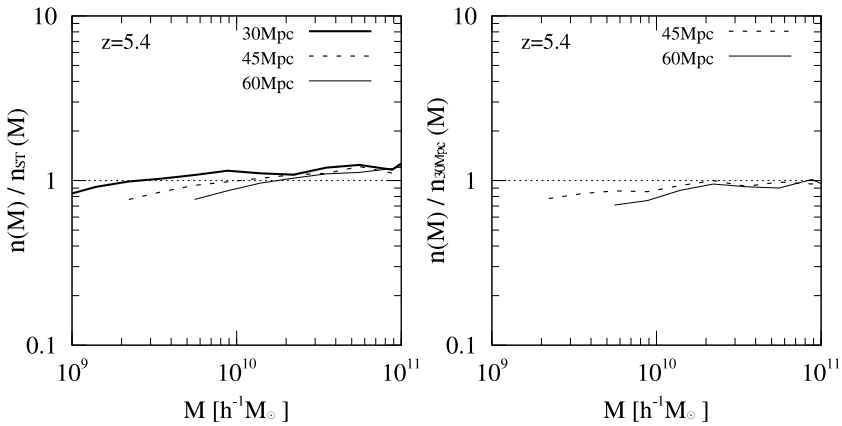

Figure 5. Left panel shows three mass functions at $z = 5.4$ derived from 512^3 simulations of 30, 45, and 60 Mpc boxes, relative to the Sheth & Tormen (1999) function. Right panel shows mass functions of 45 and 60 Mpc box simulations, relative to that of the 30 Mpc box simulation.

First, we determine the minimum number of particles in a halo necessary to reliably determine the concentration. Figure 8 shows the normalized difference of average concentration between the G2048 run and the CG512 run as a function of halo mass. We can see that the difference is ∼0.05 for the halo mass larger than $3.0 \times 10^{10}\ M_{\odot}$. For halo mass less than $3.0 \times 10^{10}\ M_{\odot}$, the difference is larger. In the CG512 run, a halo of mass $3.0 \times 10^{10}\ M_{\odot}$ contains ∼4000 particles. So we conclude that we need ∼4000 particles to reliably determine the concentration. For the CG2048 run, the reliability limit is $5.0 \times 10^{8}\ M_{\odot}$.

Figure 9 shows the median and first and third quantiles of the concentration as a function of the virial mass of the halo. We can see a clear correlation between the halo mass and the concentration. Apparently, the dependence is weaker for smaller mass. Therefore, the fitting functions with a single power (e.g., Bullock et al. 2001a; Neto et al. 2007; Macciò et al. 2007; Klypin et al. 2011) cannot be used for halos of the size of dwarf galaxies.

Theoretically, the concentration of a halo reflects the cosmic density at the formation time of the halo (Bullock et al. 2001a). The concentrations of halos formed earlier are higher than those of halos formed later. However, the dependence should be weak for small halos since the dependence of the formation epoch on the halo mass is small for small (smaller than $10^{8}\ M_{\odot}$) halos. The slope of the power spectrum of initial density fluctuations approaches −3 for the small mass limit.

In Figure 9, we also plot an analytical prediction of the mass–concentration relation, obtained by the method used in Navarro et al. (1997) assuming that all halos have the NFW

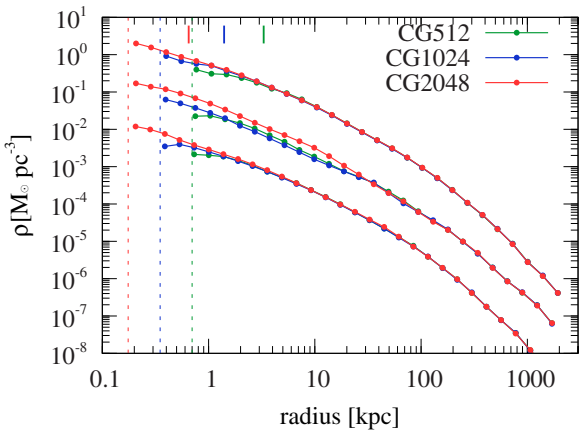

Figure 6. Spherically averaged radial density profiles of the largest three halos at $z = 0$. Two of three profiles (middle and bottom) are vertically shifted downward by 1 and 2 dex. Vertical dashed lines show the softening length of three simulations. Upside short vertical bars indicate the reliability limit of the most massive halo calculated using criteria proposed by Fukushige & Makino (2001) and Power et al. (2003). The red, blue, and green correspond to the simulation CG2048, CG1024, and CG512.

(A color version of this figure is available in the online journal.)

profile. The formation redshift z_f of halos with mass M is defined as the epoch at which progenitors with mass larger than fM first contained half of mass M. It is estimated by using the Press–Schechter formalism (e.g., Lacey & Cole 1993),

$$\mathrm{erfc}\left\{\frac{\delta_{\rm crit}(z_f)-\delta_{\rm crit}(0)}{\sqrt{2\left[\sigma_0^2(fM)-\sigma_0^2(M)\right]}}\right\}=\frac{1}{2}, \tag{3}$$

where $\delta_{\rm crit}(z)$ is the critical overdensity for the spherical collapse at z_f, and $\sigma_0^2(M)$ is the variance of the density fluctuation at $z = 0$ smoothed by a top-hat filter on a mass scale of M. Here, we used $f = 0.01$. The characteristic density ρ_0 of a halo should reflect the cosmic density at the formation time. Thus, we assume

$$\rho_0 = \rho_{\rm norm}\,(1+z_f)^3\,, \tag{4}$$

where $\rho_{\rm norm}$ is chosen to fit the simulation results. The mass of a halo with the NFW profile is given by

$$M = 4\pi\rho_0 r_s^3\left[\ln(1+c)-c/(1+c)\right]. \tag{5}$$

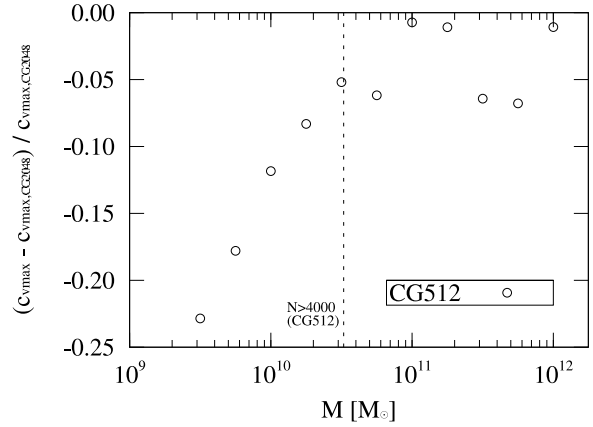

Figure 8. Residuals of concentration $c_{\rm vmax} = R_{\rm vir}/R_{\rm vmax}$ from the largest simulation (CG2048) to the lower resolution simulation (CG512).

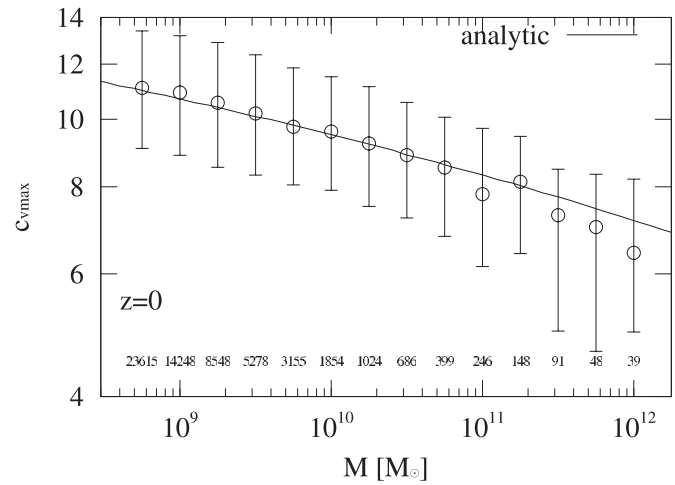

Figure 9. Concentration plotted against the halo virial mass M at $z = 0$. Circles show the median value on each bin. Whiskers are the first and third quantiles. The number of halos on each bin is shown below circles. Thick solid line shows the result from an analytical model.

The mass and concentration at $z = 0$ are related to each other by

$$M = \frac{4}{3}\pi R_{\rm vir}^3\Delta(0)\rho_{\rm crit} = \frac{4}{3}\pi r_s^3 c^3\Delta(0)\rho_{\rm crit}, \tag{6}$$

where $\rho_{\rm crit}$ is the critical density. From Equations (1), (3), (4), (5), and (6), we can analytically estimate the concentration of halos with mass M.

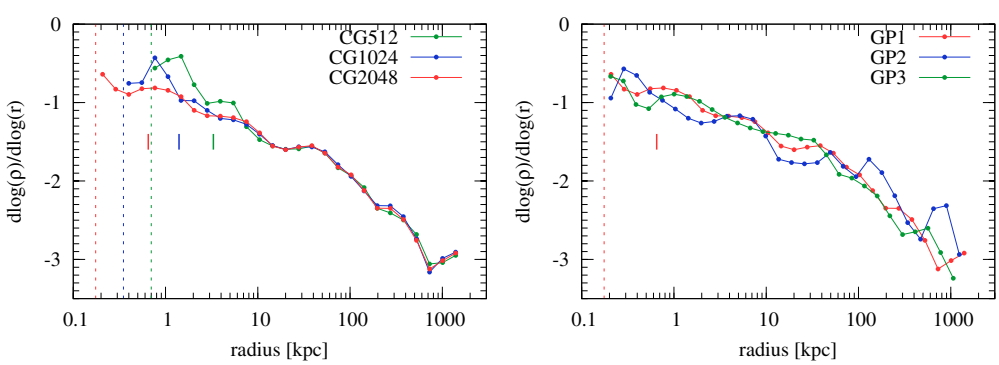

Figure 7. Slopes of radial density profiles of the largest three halos at $z = 0$. Left panel shows those of the largest halo for three different resolutions. Right panel shows those of the largest three halos for the largest simulation (CG2048).

(A color version of this figure is available in the online journal.)

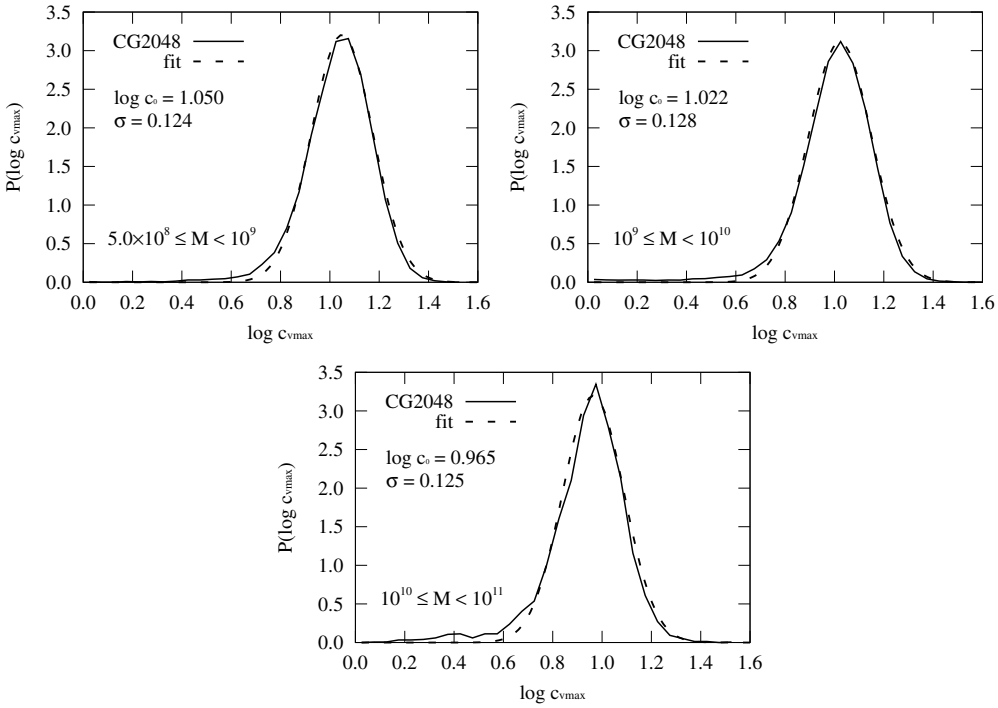

Figure 10. Probability distribution functions of the concentration at $z = 0$. These panels show the results of different mass ranges. Dashed curves are the best fits of the log-normal distribution.

As mentioned by Lacey & Cole (1993), the estimated formation epoch obtained using Equation (3) is not necessarily correct. This is because the formation time defined here corresponds to the epoch at which one of the progenitors has a mass larger than fM. This does not mean that the main progenitor has this mass. Nevertheless, as seen in Figure 9, the analytical prediction based on Equation (3) shows a very good agreement with the result from the CG2048 run for halos with mass smaller than $10^{11}\,M_\odot$. For halos with mass larger than $10^{11}\,M_\odot$, the difference between CG2048 results and analytical ones is relatively large. However, these halos are rare objects in the CG2048 run, which might affect the results in some degree. We can conclude that the shallowing slope of the mass–concentration relation naturally emerges from the nature of the power spectrum of initial density fluctuations.

The slope is slightly shallower than that of $c_{\rm NFW}$ for larger halos. For the case of $c_{\rm NFW}$, the slope is around -0.10 for relaxed halos and -0.11 for all halos (Neto et al. 2007; Macciò et al. 2007). On the other hand, for the CG2048 simulation, the slope is around -0.07 for halos with mass $10^{10}\,M_\odot$, and -0.06 for halos with mass $10^9\,M_\odot$. Note that one overestimates the central density of halos if one estimates the concentration of dwarf-sized halos by extrapolating the mass–concentration relation of galaxy- or cluster-sized halos.

Figure 10 shows the probability distribution functions of the concentration parameter at $z = 0$ in three different mass ranges. Both shapes are well fitted by the log-normal distributions,

$$P(\log c_{\rm vmax}) = \frac{1}{\sqrt{2\pi}\sigma}\exp\left(-\frac{\log^2(c_{\rm vmax}/c_0)}{2\sigma^2}\right). \quad (7)$$

We find $\log c_0 = 1.050, \sigma = 0.124$ for halos with mass of $5.0\times10^8\,M_\odot \leqslant M < 10^9\,M_\odot$, $\log c_0 = 1.022, \sigma = 0.128$ for halos with mass of $10^9\,M_\odot \leqslant M < 10^{10}\,M_\odot$, and $\log c_0 = 0.965, \sigma = 0.125$ for halos with mass of $10^{10}\,M_\odot \leqslant M < 10^{11}\,M_\odot$.

3.4. Spin Distributions

The dimensionless spin parameter is a good parameter to quantify the rotation of a halo. One often uses the spin parameter defined in Bullock et al. (2001a),

$$\lambda = \frac{J}{\sqrt{2}MVR}, \quad (8)$$

where M, R, V, and J are the virial mass of the halo, radius, rotational velocity at R, and total angular momentum inside R.

The distribution, the dependence on the halo mass, and the evolution have been studied by a number of works (e.g., Bullock et al. 2001a; Bailin & Steinmetz 2005; Bett et al. 2007; Macciò et al. 2007, 2008; Knebe & Power 2008; Antonuccio-Delogu et al. 2010; Muñoz-Cuartas et al. 2011; Wang et al. 2011). The spin of galaxy-sized halos is well studied by using the results of sufficient resolution simulations. However, we do not understand those of dwarf-galaxy-sized halos. The spin distribution of those halos at only high redshifts is studied by the result of high-resolution simulations (Knebe & Power 2008). Here, we extend the spin distributions at $z = 0$ to dwarf-galaxy-sized halos (down to $10^8\,M_\odot$) in the same way as the concentration.

First, we determine the minimum number of particles in a halo necessary to reliably determine the spin as done for the concentration. Figure 11 shows the normalized difference of average spin between the CG2048 run and the CG512 run as a function of halo mass. We can see that the difference is $\sim$0.05 for halo mass larger than $8.0\times10^9\,M_\odot$. For halo mass less than $8.0\times10^9\,M_\odot$, the difference is large. In the CG512 run, a halo of mass $8.0\times10^9\,M_\odot$ contains $\sim$1000 particles. So we conclude that we need $\sim$1000 particles to reliably determine the concentration. For the CG2048 run, the reliability limit is $1.28\times10^8 M_\odot$.

Figure 12 shows the median and first and third quantiles of the spin parameter as a function of the virial mass of the halo.

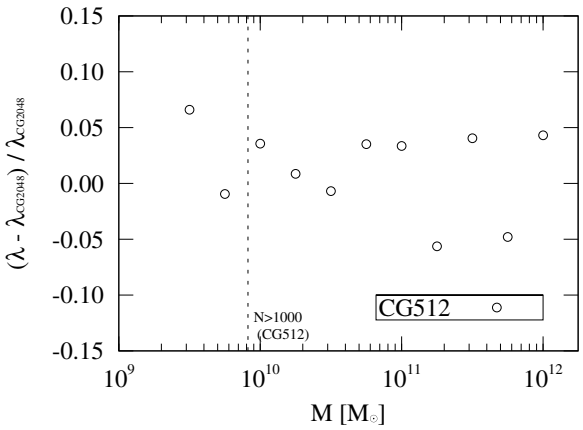

Figure 11. Residuals of spin from the largest simulation (CG2048) to lower resolution simulation (CG512).

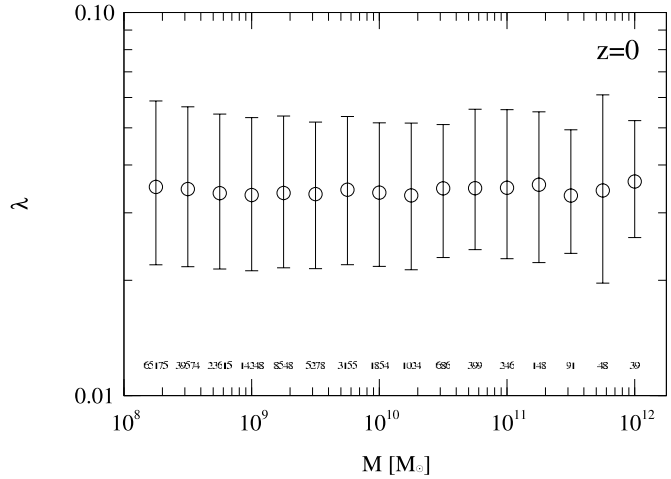

Figure 12. Spin parameter λ plotted against the halo virial mass M at $z = 0$. Circles show the median value on each bin. Whiskers are the first and third quantiles. The number of halos on each bin is shown below circles.

Apparently, we can see the spin parameter is independent of the mass down to $10^8\ M_\odot$ as pointed out for larger halos in previous works (Macciò et al. 2007; Muñoz-Cuartas et al. 2011). The median value is 0.0336.

Figure 13 shows the probability distribution functions of the spin parameter at $z = 0$ in three different mass ranges. The distributions are well fitted by the log-normal distributions,

$$P(\log\lambda) = \frac{1}{\sqrt{2\pi}\sigma}\exp\left(-\frac{\log^2(\lambda/\lambda_0)}{2\sigma^2}\right). \quad (9)$$

We find $\log\lambda_0 = -1.477, \sigma = 0.308$ for halos with mass of $1.28 \times 10^8\ M_\odot \leqslant M < 10^9\ M_\odot$, $\log\lambda_0 = -1.480, \sigma = 0.288$ for halos with mass of $10^9\ M_\odot \leqslant M < 10^{10}\ M_\odot$, and $\log\lambda_0 = -1.472, \sigma = 0.277$ for halos with mass of $10^{10}\ M_\odot \leqslant M < 10^{11}\ M_\odot$. Thus, we conclude that there is no mass dependence of the spin parameter. Otherwise, it is extremely weak.

We can see that there are small deviations from the log-normal distributions at high spin regions as seen in previous works for larger halos (Bett et al. 2007; Antonuccio-Delogu et al. 2010). We will discuss the effect of the dynamical state of halos in the Appendix.

3.5. Subhalo

The statistics of the subhalo abundance of galaxy-sized halos have been well studied (e.g., Ishiyama et al. 2009b; Boylan-Kolchin et al. 2010; Busha et al. 2011). The subhalo abundance shows large halo-to-halo variations and depends on the concentration parameter. Halos with larger concentrations have a smaller number of subhalos. This means that the number of subhalos should increase as the halo mass increases since the concentration decreases. However, little is known on how the subhalo abundance depends on the halo mass. The reason is that we need a number of well-resolved halos in a wide mass range to determine the mass dependence and it is computationally expensive to perform simulations for this purpose.

Contini et al. (2012) analyzed the fraction of halo mass in subhalos for group-sized to cluster-sized halos and showed that the fraction increases with increasing mass. For group-sized halos, it is approximately 5%, and for cluster-sized halos approximately 10% (similar results are obtained in Gao et al. 2011 for a slightly different mass range). However, the number of particles per halo of their group-sized halos is 10^5, which is insufficient to robustly estimate the subhalo abundance (see also Ishiyama et al. 2009b). Therefore, it is possible that they have underestimated the subhalo abundance.

Our high-resolution simulations are suitable for the study of the statistics of the subhalo abundance for halos with smaller mass. Therefore we can address a key question, how the subhalo abundance depends on the halo mass. Hereafter, we define $N_{>x}$ as the subhalo abundance, which is the number of subhalos with rotation velocity larger than x times that of the parent halo. Figure 14 shows the normalized difference of average subhalo abundance between the CG2048 run and the CG1024 run as a function of halo mass for $x = 0.10, 0.125, 0.15$. We can see that both results are well converged for halos with more than one million particles for all values of x. For halos with less particles, the difference becomes larger as the halo mass decreases. Thus, we can conclude that we need about one million particles to reliably determine the subhalo abundance. For the CG2048 run, the reliability limit is $1.28 \times 10^{11}\ M_\odot$ for $x = 0.1$.

The reliability limit should be smaller for larger subhalos (larger values of x) since they consist of more particles than smaller ones. As seen in Figure 14, the residual of the subhalo abundance is systematically smaller for larger subhalos (larger x). However, for simplicity, we use the same reliability limit for all values of x. Thus, our choice of the reliability limit is quite conservative.

Figure 15 shows the mean and the standard deviation of the subhalo abundance as a function of the virial mass of the halo. We can see clearly that the subhalo abundance depends on the halo mass for all values of x. The average number of subhalos $N_{>0.10}$, $N_{>0.125}$, $N_{>0.15}$ are 30.1, 16.5, 9.3 for halos with mass of $\sim 2 \times 10^{11}\ M_\odot$ and 47.0, 23.8, 13.7 for halos with mass of $\sim 1 \times 10^{12}\ M_\odot$. For halos with mass larger than $\sim 1 \times 10^{12}\ M_\odot$, we can see that the dependence becomes weaker and gradually approaches a constant value.

This trend has not been observed in previous works (Gao et al. 2011; Contini et al. 2012), since they analyzed halos with larger mass. However, our result is limited by the box size of the simulation. Since the number of subhalos with mass larger than $1 \times 10^{12}\ M_\odot$ in our simulation is only 82, our halos within this mass range might be a biased sample. In order to clarify the dependency, larger box simulations are needed.

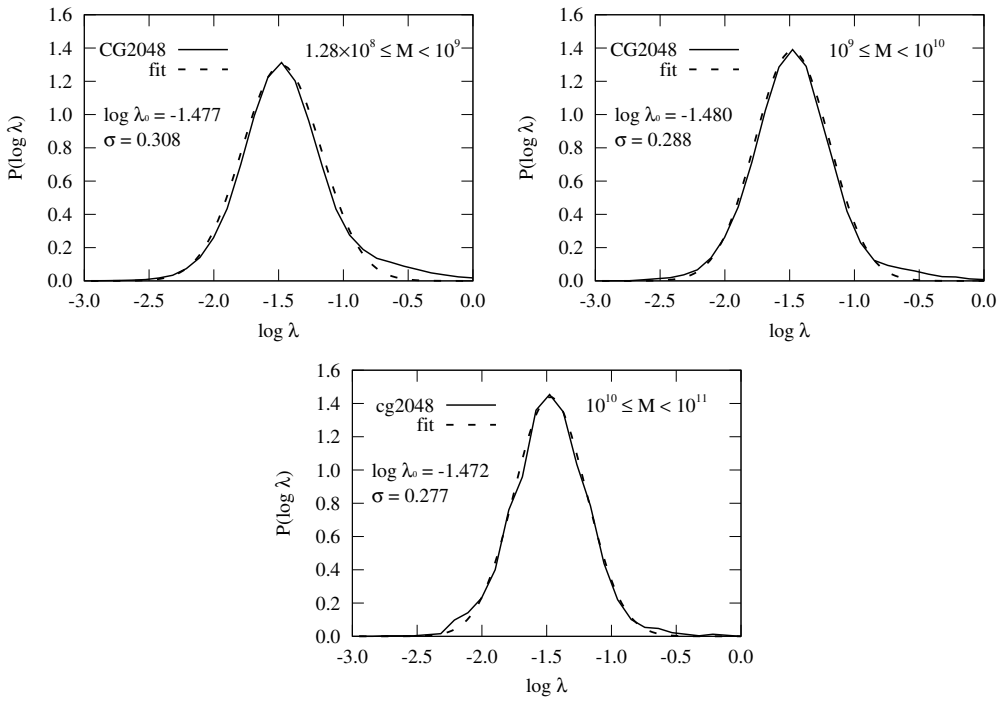

Figure 13. Probability distribution functions of the spin parameter at $z = 0$. These panels show the results of different mass ranges. Dashed curves are the best fits of the log-normal distribution.

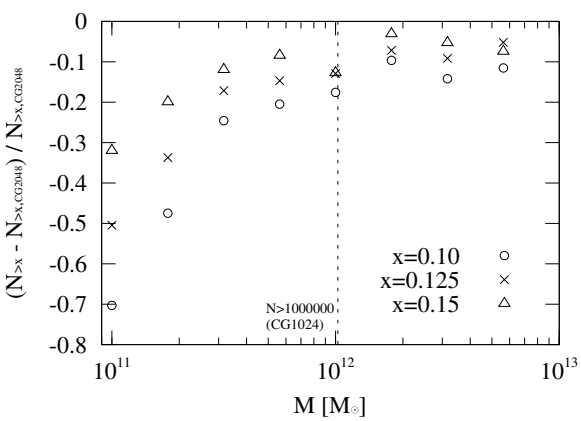

Figure 14. Residuals of the subhalo abundance from the largest simulation (CG2048) to lower resolution simulation (CG1024). Here, $N_{>x}$ is the number of subhalos with rotation velocity larger than x of that of the parent halo.

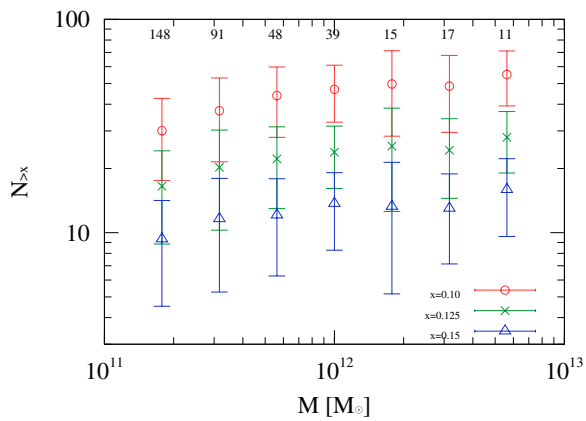

Figure 15. Number of subhalos plotted against the halo virial mass M at $z = 0$. Each symbol shows the mean value on each bin. Whiskers are the standard deviation. The number of halos on each bin is shown above.

(A color version of this figure is available in the online journal.)

4. DISCUSSIONS AND SUMMARY

We present the first scientific results of the Cosmogrid simulation. Because of unprecedentedly high resolution and powerful statistics, the simulation is suitable to resolve internal properties of halos with mass larger than dwarf galaxies and subhalos whose scales are comparable to ultra-faint dwarf galaxies.

We summarize the main results of this paper as follows.

1. The halo mass function is well described by the Sheth & Tormen (1999) fitting function down to $\sim 10^7\ M_\odot$ from $1.0 \times 10^{13}\ M_\odot$. The differences are less than 10% at $z = 0$ from $M = 5.0 \times 10^7\ M_\odot$ to $M = 2.0 \times 10^{12}\ M_\odot$.
2. We analyzed the spherically averaged density profiles of the three most massive halos which contain more than 170 million particles. Their masses are 5.24, 3.58, and $2.25 \times 10^{13}\ M_\odot$. We confirmed that the slopes of density profiles of these halos become shallower than -1 at the innermost radius. The results are consistent with the recent studies based on high-resolution simulations for galactic halos.
3. We studied internal properties of halos at $z = 0$ with mass more than $\sim 10^8\ M_\odot$. The concentration parameter measured by the maximum rotational velocity radius is weakly correlated with the halo mass. We found that the dependence of the concentration parameter with halo mass cannot be expressed by a single power law, but levels off at small mass. The slope of the mass–concentration relation is around -0.07 for halos with mass $10^{10}\ M_\odot$, and

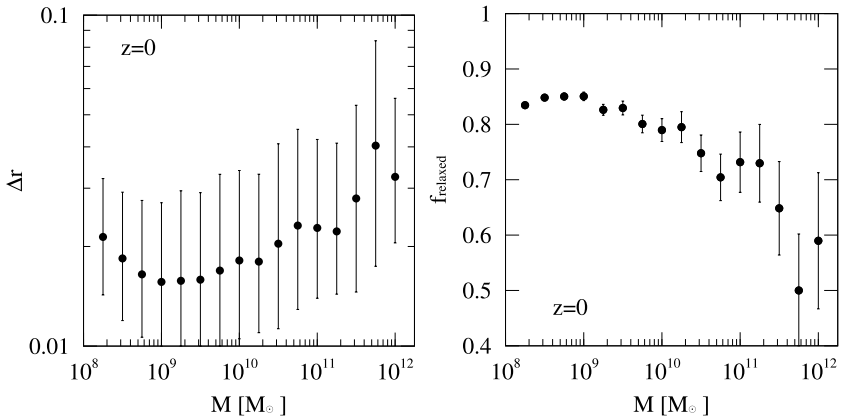

Figure 16. Left: the center-of-mass offset of all halos plotted against the halo virial mass M at $z = 0$. The median value of each bin is shown by circles. Whiskers are the first and third quantiles. Right: the fraction of relaxed halos. Error bars are Poisson errors.

-0.06 for halos with mass $10^9\ M_\odot$. The shallowing slope naturally emerges from the nature of the power spectrum of initial density fluctuations. A simple model based on the Press–Schechter theory gives reasonable agreement with the simulation result. The spin parameter does not show a correlation with the halo mass. The probability distribution functions of concentration and spin are well fitted by the log-normal distribution for halos with mass larger than $\sim 10^8\ M_\odot$.

4. The subhalo abundance depends on the halo mass. Galaxy-sized halos have 50% more subhalos than $\sim 10^{11}\ M_\odot$ halos have. We find a new result that the dependence becomes weaker for more massive halos.

We thank the anonymous referee for his/her valuable comments. Numerical computations were partially carried out on Cray XT4 at Center for Computational Astrophysics, CfCA, of National Astronomical Observatory of Japan, the K computer at the RIKEN Advanced Institute for Computational Science (Proposal number hp120286), Huygens at the Dutch National High Performance Computing and e-Science Support Center, SARA (Netherlands), HECToR at the Edinburgh Parallel Computing Center (United Kingdom), and Louhi at IT Center for Science in Espoo (Finland). T.I. is financially supported by Research Fellowship of the Japan Society for the Promotion of Science (JSPS) for Young Scientists. This research is partially supported by the Special Coordination Fund for Promoting Science and Technology (GRAPE-DR project), Ministry of Education, Culture, Sports, Science and Technology, Japan. We also thank the network facilities of SURFnet, DEISA, IEEAF, WIDE, Northwest Gigapop and the Global Lambda Integrated FAcility (GLIF) GOLE of TransLight Cisco on National LambdaRail, Trans- Light, StarLight, NetherLight, T-LEX, Pacific and Atlantic Wave. This research is supported by the Netherlands organization for Scientific research (NWO) grant Nos. 639.073.803, 643.200.503 and 643.000.803, the Stichting Nationale Computerfaciliteiten (project SH-095-08), NAOJ, SURFnet (GigaPort project), the International Information Science Foundation (IISF), the Netherlands Advanced School for Astronomy (NOVA), and the Leids Kerkhoven-Bosscha fonds (LKBF). We thank the DEISA Consortium (EU FP6 project RI-031513 and FP7 project RI-222919) for support within the DEISA Extreme Computing Initiative (GBBP project). This work has been funded by MEXT HPCI STRATEGIC PROGRAM and MEXT/JSPS KAKENHI Grand Number 24740115.

APPENDIX

THE EFFECT OF DYNAMICAL STATE OF HALOS

There are large variations in the dynamical state of halos. Halos which formed in an early epoch tend to be dynamically relaxed, whereas halos which experienced a recent major merger tend to be dynamically unrelaxed. The relaxation state of halos might have some effect on properties of halos such as the concentration and the spin. Here, we analyze these properties for only the dynamically relaxed sample of halos and discuss the effect of the relaxation state.

Power et al. (2012) argued that the center-of-mass offset is a robust estimator of the relaxation state of halos. The center-of-mass offset is defined as

$$\Delta r = \frac{|\boldsymbol{r}_{\rm cen} - \boldsymbol{r}_{\rm cm}|}{R_{\rm vir}}, \tag{A1}$$

where $\boldsymbol{r}_{\rm cen}$, $\boldsymbol{r}_{\rm cm}$, and $R_{\rm vir}$ are the center of density, mass, and the virial radius of a halo. They found that $\Delta r \leqslant 0.04$ is a sufficient condition to pick up dynamically relaxed halos at $z = 0$. We use this condition to construct the relaxed sample of halos from our all halo samples.

Figure 16 shows the average center-of-mass offset and the fraction of relaxed halos as a function of the halo virial mass. The offset increases with increasing halo mass. This trend is in good agreement with the results of Power et al. (2012). It is simply because lower mass halos tend to form earlier than higher mass halos from the nature of the hierarchical structure formation. As a result, the fraction of relaxed halos becomes large for lower mass halos. We can see the offset increases with decreasing halo mass from $\sim 5 \times 10^8\ M_\odot$. This may be caused by the resolution effect.

One may wonder whether the dependence of concentrations on the halo mass is caused by unrelaxed halos or not. Figure 17 shows the median concentration and spin for all and the relaxed sample of halos as a function of the virial mass of the halo. The relaxation state has little impact on the concentration for halos smaller than $10^{11}\ M_\odot$. This can be interpreted as the fact that the fraction of relaxed halos is large for lower mass halos as we can see in Figure 16.

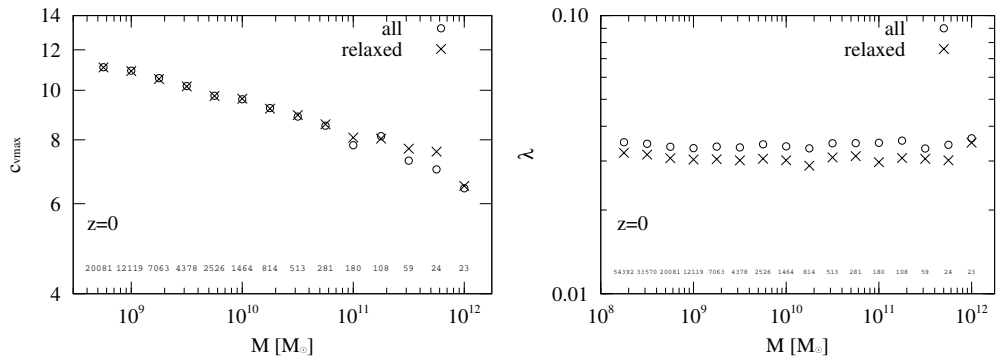

Figure 17. Concentration (left) and spin (right) plotted against the halo virial mass M at $z = 0$. The median values of all halos are shown by circles. Crosses are for the values of only relaxed halos. The number of relaxed halos on each bin is shown below.

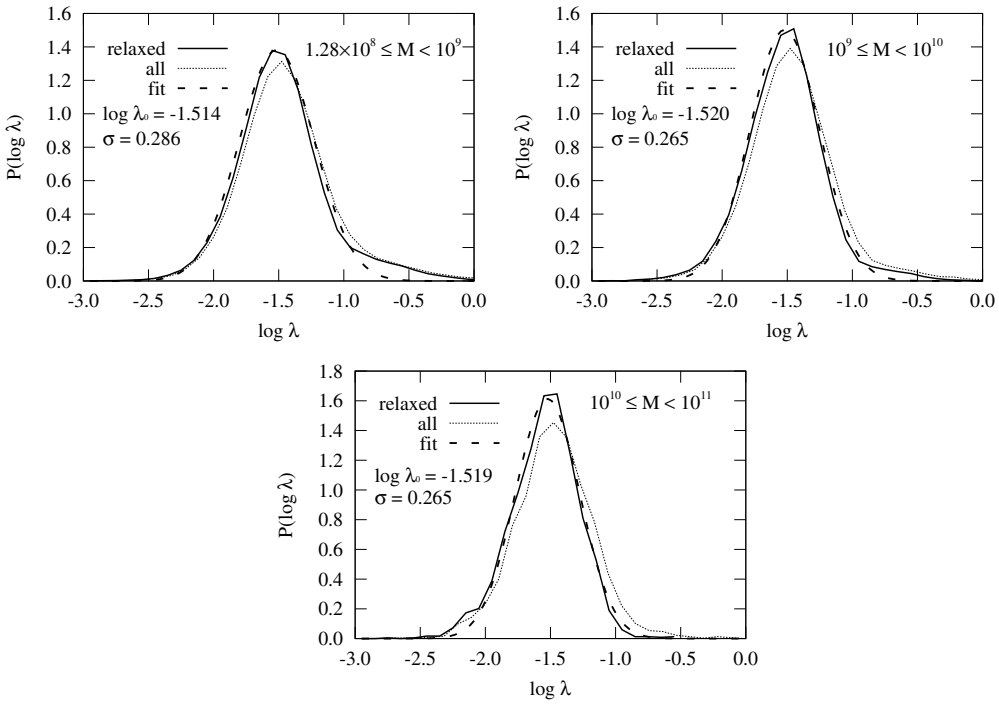

Figure 18. Probability distribution functions of the spin parameter at $z = 0$ for relaxed halos (solid) and all halos (dotted). Dashed curves are the best fits of the log-normal distribution for relaxed halos.

The spin parameters of relaxed halos are systematically smaller than those of all halos by ∼8%–10% for all mass ranges. This result is consistent with early studies (Macciò et al. 2007, 2008). This is because unrelaxed halos tend to experience a recent major merger, giving them higher spin values. Figure 18 shows the probability distribution functions of the spin parameter at $z = 0$ in three different mass ranges. We can see clearly that the number of halos with high spin values in the relaxed sample of halos is smaller than that in the all sample of halos for all mass ranges. We find $\log \lambda_0 = -1.514, \sigma = 0.286$ for halos with mass of $1.28 \times 10^8\ M_\odot \leqslant M < 10^9\ M_\odot$, $\log \lambda_0 = -1.520, \sigma = 0.265$ for halos with mass of $10^9\ M_\odot \leqslant M < 10^{10}\ M_\odot$, and $\log \lambda_0 = -1.519, \sigma = 0.265$ for halos with mass of $10^{10}\ M_\odot \leqslant M < 10^{11}\ M_\odot$. The standard deviations are also systematically smaller for relaxed halos by ∼4%–8%.

Small deviations from the log-normal distributions at high spin regions for all halos are also seen for relaxed halos. The deviations become weaker since unrelaxed halos with higher spin are removed.

It is interesting that the spin is relatively influenced by the relaxation state more than the concentration. This might be because halos grow in a self-similar way (e.g., Fukushige & Makino 2001). The self-similar growth means that the inner region of a halo forms earlier than the outer region. Here, the spin is calculated using all particles. The concentration is estimated using particles within the radius of the maximum rotational velocity, which should be more dynamically relaxed than particles in the outer region. Therefore, it is natural that the effect of the relaxation state on the concentration and spin shows such difference.

In summary, we find that the relaxation state makes small difference on the concentration and spin distributions.

1. The impact of the relaxation state on the concentration is negligible for halos smaller than $10^{11}\ M_\odot$.
2. The spin parameters of relaxed halos are systematically smaller than those of all halos by ∼8%–10% for all mass ranges. The spin distributions of relaxed halos deviate from the log-normal fitting less than those of all halos.

REFERENCES

Aarseth, S. J., Turner, E. L., & Gott, J. R., III. 1979, ApJ, 228, 664
Antonuccio-Delogu, V., Dobrotka, A., Becciani, U., et al. 2010, MNRAS, 407, 1338
Bagla, J. S., & Prasad, J. 2006, MNRAS, 370, 993
Bailin, J., & Steinmetz, M. 2005, ApJ, 627, 647
Barnes, J., & Hut, P. 1986, Natur, 324, 446
Bertschinger, E. 2001, ApJS, 137, 1
Bett, P., Eke, V., Frenk, C. S., et al. 2007, MNRAS, 376, 215
Boylan-Kolchin, M., Springel, V., White, S. D. M., & Jenkins, A. 2010, MNRAS, 406, 896
Boylan-Kolchin, M., Springel, V., White, S. D. M., Jenkins, A., & Lemson, G. 2009, MNRAS, 398, 1150
Bryan, G. L., & Norman, M. L. 1998, ApJ, 495, 80
Bullock, J. S., Dekel, A., Kolatt, T. S., et al. 2001a, ApJ, 555, 240
Bullock, J. S., Kolatt, T. S., Sigad, Y., et al. 2001b, MNRAS, 321, 559
Busha, M. T., Wechsler, R. H., Behroozi, P. S., et al. 2011, ApJ, 743, 117
Contini, E., De Lucia, G., & Borgani, S. 2012, MNRAS, 420, 2978
Crocce, M., Fosalba, P., Castander, F. J., & Gaztañaga, E. 2010, MNRAS, 403, 1353
Diemand, J., Kuhlen, M., & Madau, P. 2007, ApJ, 657, 262
Diemand, J., Kuhlen, M., Madau, P., et al. 2008, Natur, 454, 735
Diemand, J., Moore, B., & Stadel, J. 2004, MNRAS, 353, 624
Diemand, J., Zemp, M., Moore, B., Stadel, J., & Carollo, C. M. 2005, MNRAS, 364, 665
Efstathiou, G. 1979, MNRAS, 187, 117
Evrard, A. E., MacFarland, T. J., Couchman, H. M. P., et al. 2002, ApJ, 573, 7
Fall, S. M. 1978, MNRAS, 185, 165
Fukushige, T., Kawai, A., & Makino, J. 2004, ApJ, 606, 625
Fukushige, T., & Makino, J. 1997, ApJL, 477, L9
Fukushige, T., & Makino, J. 2001, ApJ, 557, 533
Fukushige, T., & Makino, J. 2003, ApJ, 588, 674
Gao, L., Frenk, C. S., Boylan-Kolchin, M., et al. 2011, MNRAS, 410, 2309
Gao, L., Navarro, J. F., Cole, S., et al. 2008, MNRAS, 387, 536
Gao, L., White, S. D. M., Jenkins, A., Stoehr, F., & Springel, V. 2004, MNRAS, 355, 819
Ghigna, S., Moore, B., Governato, F., et al. 2000, ApJ, 544, 616
Graham, A. W., Merritt, D., Moore, B., Diemand, J., & Terzić, B. 2006, AJ, 132, 2701
Groen, D., Portegies Zwart, S., Ishiyama, T., & Makino, J. 2011, CS&D, 4, 015001
Groen, D., Rieder, S., Grosso, P., de Laat, C., & Portegies Zwart, S. 2010, CS&D, 3, 015002
Hayashi, E., Navarro, J. F., Power, C., et al. 2004, MNRAS, 355, 794
Hockney, R. W., & Eastwood, J. W. 1981, Computer Simulation Using Particles (New York: McGraw-Hill)
Ishiyama, T., Fukushige, T., & Makino, J. 2008, PASJ, 60, L13
Ishiyama, T., Fukushige, T., & Makino, J. 2009a, PASJ, 61, 1319
Ishiyama, T., Fukushige, T., & Makino, J. 2009b, ApJ, 696, 2115
Jenkins, A., Frenk, C. S., White, S. D. M., et al. 2001, MNRAS, 321, 372
Jing, Y. P. 2000, ApJ, 535, 30
Jing, Y. P., & Suto, Y. 2000, ApJL, 529, L69
Jing, Y. P., & Suto, Y. 2002, ApJ, 574, 538
Kawai, A., Makino, J., & Ebisuzaki, T. 2004, ApJS, 151, 13
Kazantzidis, S., Zentner, A. R., & Kravtsov, A. V. 2006, ApJ, 641, 647
Kim, J., Park, C., Gott, J. R., & Dubinski, J. 2009, ApJ, 701, 1547
Klypin, A., Kravtsov, A. V., Bullock, J. S., & Primack, J. R. 2001, ApJ, 554, 903
Klypin, A., Kravtsov, A. V., Valenzuela, O., & Prada, F. 1999, ApJ, 522, 82
Klypin, A. A., Trujillo-Gomez, S., & Primack, J. 2011, ApJ, 740, 102
Knebe, A., & Power, C. 2008, ApJ, 678, 621
Kroupa, P., Famaey, B., de Boer, K. S., et al. 2010, A&A, 523, A32
Lacey, C., & Cole, S. 1993, MNRAS, 262, 627
Lacey, C., & Cole, S. 1994, MNRAS, 271, 676
Li, Y., Helmi, A., De Lucia, G., & Stoehr, F. 2009, MNRAS, 397, L87
Lukić, Z., Heitmann, K., Habib, S., Bashinsky, S., & Ricker, P. M. 2007, ApJ, 671, 1160
Macciò, A. V., Dutton, A. A., & van den Bosch, F. C. 2008, MNRAS, 391, 1940
Macciò, A. V., Dutton, A. A., van den Bosch, F. C., et al. 2007, MNRAS, 378, 55
Macciò, A. V., Kang, X., & Moore, B. 2009, ApJL, 692, L109
Makino, J. 2004, PASJ, 56, 521
Merritt, D., Graham, A. W., Moore, B., Diemand, J., & Terzić, B. 2006, AJ, 132, 2685
Miyoshi, K., & Kihara, T. 1975, PASJ, 27, 333
Moore, B., Ghigna, S., Governato, F., et al. 1999a, ApJL, 524, L19
Moore, B., Quinn, T., Governato, F., Stadel, J., & Lake, G. 1999b, MNRAS, 310, 1147
Muñoz-Cuartas, J. C., Macciò, A. V., Gottlöber, S., & Dutton, A. A. 2011, MNRAS, 411, 584
Navarro, J. F., Frenk, C. S., & White, S. D. M. 1997, ApJ, 490, 493
Navarro, J. F., Hayashi, E., Power, C., et al. 2004, MNRAS, 349, 1039
Navarro, J. F., Ludlow, A., Springel, V., et al. 2010, MNRAS, 402, 21
Neto, A. F., Gao, L., Bett, P., et al. 2007, MNRAS, 381, 1450
Okamoto, T., & Frenk, C. S. 2009, MNRAS, 399, L174
Peacock, J. A. 1999, Cosmological Physics (Cambridge, UK: Cambridge Univ. Press)
Portegies Zwart, S., Ishiyama, T., Groen, D., et al. 2010, IEEE Computer, 43, 63
Power, C., & Knebe, A. 2006, MNRAS, 370, 691
Power, C., Knebe, A., & Knollmann, S. R. 2012, MNRAS, 419, 1576
Power, C., Navarro, J. F., Jenkins, A., et al. 2003, MNRAS, 338, 14
Press, W. H., & Schechter, P. 1974, ApJ, 187, 425
Prunet, S., Pichon, C., Aubert, D., et al. 2008, ApJS, 178, 179
Reed, D., Gardner, J., Quinn, T., et al. 2003, MNRAS, 346, 565
Reed, D., Governato, F., Verde, L., et al. 2005, MNRAS, 357, 82
Reed, D. S., Bower, R., Frenk, C. S., Jenkins, A., & Theuns, T. 2007, MNRAS, 374, 2
Reed, D. S., Koushiappas, S. M., & Gao, L. 2011, MNRAS, 415, 3177
Sheth, R. K., & Tormen, G. 1999, MNRAS, 308, 119
Springel, V., Wang, J., Vogelsberger, M., et al. 2008, MNRAS, 391, 1685
Springel, V., White, S. D. M., Jenkins, A., et al. 2005, Natur, 435, 629
Stadel, J., Potter, D., Moore, B., et al. 2009, MNRAS, 398, L21
Strigari, L. E., Bullock, J. S., Kaplinghat, M., et al. 2008, Natur, 454, 1096
Taylor, J. E., & Navarro, J. F. 2001, ApJ, 563, 483
Teyssier, R., Pires, S., Prunet, S., et al. 2009, A&A, 497, 335
Tinker, J., Kravtsov, A. V., Klypin, A., et al. 2008, ApJ, 688, 709
van den Bosch, F. C., Tormen, G., & Giocoli, C. 2005, MNRAS, 359, 1029
Wambsganss, J., Bode, P., & Ostriker, J. P. 2004, ApJL, 606, L93
Wang, H., Mo, H. J., Jing, Y. P., Yang, X., & Wang, Y. 2011, MNRAS, 413, 1973
Warren, M. S., Abazajian, K., Holz, D. E., & Teodoro, L. 2006, ApJ, 646, 881
Wechsler, R. H., Bullock, J. S., Primack, J. R., Kravtsov, A. V., & Dekel, A. 2002, ApJ, 568, 52
White, M., Cohn, J. D., & Smit, R. 2010, MNRAS, 408, 1818
White, S. D. M., & Rees, M. J. 1978, MNRAS, 183, 341
Yahagi, H., Nagashima, M., & Yoshii, Y. 2004, ApJ, 605, 709
Yoshikawa, K., & Fukushige, T. 2005, PASJ, 57, 849
Zentner, A. R., Berlind, A. A., Bullock, J. S., Kravtsov, A. V., & Wechsler, R. H. 2005, ApJ, 624, 505
Zhao, D. H., Jing, Y. P., Mo, H. J., & Börner, G. 2003, ApJL, 597, L9
Zhao, D. H., Jing, Y. P., Mo, H. J., & Börner, G. 2009, ApJ, 707, 354